Polymer 300 (2024) 126907

Contents lists available at ScienceDirect

Polymer

journal homepage: www.elsevier.com/locate/polymer

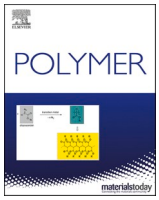

Thermomechanical characterisation of polyamide 6 over a wide range of rates and temperatures

Peihao Song [a,b], Akash Trivedi [a,b], Nicholas Hawkins [a], Aaron Graham [a,b], David Chapman [a,b], Clive R. Siviour [a,*]

[a] Department of Engineering Science, University of Oxford, Parks Road, OX1 3PJ, UK
[b] DPI, P.O. Box 902, 5600 AX, Eindhoven, the Netherlands

ARTICLE INFO

Keywords:
Polyamide 6
Thermomechanical characterisation
Rate- and temperature-dependence

ABSTRACT

Polyamide 6 is a widely used engineering plastic; however, its thermomechanical properties are not well understood, particularly at medium and high strain rates. In this research, the thermomechanical properties of Polyamide 6 were extensively characterized. Differential Scanning Calorimetry was performed to investigate the glass transition temperature and crystallinity. Frequency sweep Dynamic Mechanical Analysis was carried out through the secondary- and glass-transitions, and the temperature dependent storage moduli obtained from different sweep frequencies were used to construct a master curve. Quasi-static tensile tests at two loading speeds were conducted with digital image correlation for full-field strain mapping. Compression properties were measured at strain rates between 0.001 and 6000 s^{-1} at room temperature, and temperatures between −60 and 200 °C at 0.01 s^{-1}. The mechanical response is highly rate- and temperature-dependent; at large strains and elevated rates, apparent softening occurs owing to heat generation, which was quantified using an infrared camera.

1. Introduction

Polyamide 6 (PA6) is a semi-crystalline engineering polymer with amide and carbonyl groups, and hydrogen bonding between chains that results in high stiffness, strength, and hygroscopicity [1]. Owing to its good mechanical performance, it is often used for sports items [2] and bearings [3], in which it can be exposed to different loading conditions, including impact. Many investigations have been performed to study molecular morphology [2–4], effect of water absorption [1,5,6] and temperature-dependent mechanical performance [1,5,7] of PA6; in particular, the rate-dependent mechanical response has been studied at quasi-static strain rates [1,7,8]. However, few investigations have addressed the high rate behaviours, e.g. above 100 s^{-1}. Furthermore, manufacturing history plays a significant role in the mechanical properties of many polymers, owing to the effect of crystallinity, and there is a need for characterisation data from consistently prepared PA6 material of known crystallinity and controlled moisture content.

The mechanical properties of polymers are sensitive to temperature and strain rate (or frequency). Dynamic Mechanical Analysis (DMA) is commonly used to measure the temperature- and frequency-dependent complex modulus, which includes the storage and loss moduli [9,10]. The glass (α)- and secondary (β)-transitions can be characterised: the mechanical performances of polymers are significantly affected by these transitions. Frequency sweep DMA data obtained at different temperatures can be used to construct a master curve with a much broader frequency or strain rate range than can be achieved directly. The master curve allows the prediction of the modulus from very low (i.e. creep) to very high (i.e. impact) strain rates. Moreover, the activation energies of the molecular transitions, such as α-and β-transitions, can be estimated using the Arrhenius relationship [11].

The tensile test is a traditional material characterisation method, and it is often used to calibrate and validate constitutive material parameters. However, separating material behaviour from the structural response is difficult, particularly when strain localisation occurs [12,13]. Digital image correlation (DIC) provides a chance to analyse the full-field deformation information, not only the overall force-displacement curve but also true stress and true strain in the localised area, at large deformations [12–16]. Song et al. [13] used full-field 2-D DIC to track local true strain changes and thereby calculate true stress using three different methods, assuming that the stretch ratio

* Corresponding author.
E-mail address: clive.siviour@eng.ox.ac.uk (C.R. Siviour).

https://doi.org/10.1016/j.polymer.2024.126907
Received 23 January 2024; Received in revised form 7 March 2024; Accepted 10 March 2024
Available online 28 March 2024

of the incompressible sample in transverse and through-thickness directions was the same. Of course, these assumptions cause uncertainty in the calculations.

Rate dependent characterisation is typically performed in compression. Screw-driven machines are widely used to perform quasi-static (QS) tests. Conducting tests at medium strain rates (e.g. 1 to 100 s^{-1}) is challenging for all materials. The frequency of experimental acquisition is close to the natural frequency of the loading apparatus, and inertia in the apparatus must be overcome so that the specimen can be deformed at a high velocity after a rapid acceleration process [17]. Hydraulic test machines have previously been applied to measure the compressive response of an engineering polymer from 1 to about 85 s^{-1} [18]. For higher strain rates, the split Hopkinson bar (SPHB) is a mature technique to test engineering polymers; however, only a few studies of high rate properties of PA 6 are available. Walley et al. used a direct impact Hopkinson bar to achieve strain rates up to 20,000 s^{-1} [19]; Plöckl [20] employed an SHPB accompanied with DIC to measure the high rate response of rectangular specimens; Pouriayevali et al. [21] performed high rate tension and compression tests using split Hopkinson bar system to calibrate a constitutive model. An essential observation in the rate-dependent tests is that the strength, or yield stress, shows a bilinear increase with increasing strain rate for both amorphous and semi-crystalline polymers, examples of the latter include polypropylene [22], poly (ether-ether-ketone) [23] and various classes of polyethylene [24]. This is attributed to the secondary (β)-transition, whose motions are restricted in high strain rate and/or low temperature tests [25]. Investigation of these effects often makes use of time-temperature equivalence – the strength at high strain rates is observed to be the same as that at low temperature. This concept, which is also used to construct master curves of elastic properties as described above, has been applied to understand high rate behaviours by using low temperature test data for polymers including polycarbonate [17,26] and plasticized polyvinyl chloride (PVC) [18].

In addition to changes in the intrinsic material response, the adiabatic heating effect plays a significant role when considering the rate-dependent constitutive behaviours of polymers, particularly at large strains and high rates [27,28]. The increased strain rate can change the experimental conditions from isothermal to adiabatic, because the timescale of the loading is insufficient for the heat generated from plastic deformation to conduct out of the specimen into the environment [17,27]. This heat can lead to a qualitatively and quantitatively different mechanical response compared with quasi-static (isothermal) tests [18,29]. To measure temperature changes, embedded thermocouples, infrared (IR) detectors and IR cameras have been used [30,31]. Generally, embedded thermocouples can induce strain localisations in the specimens and have limited response times; IR detectors can have acquisition rates of order a few microseconds, however, can only measure one location and are very sensitive to measuring angle; IR cameras can provide the full-field thermal information during large strain deformation, and modern cameras can acquire images sufficiently quickly to obtain useful information at strain rates of a few 1000 s^{-1}.

The research presented in this paper provides a comprehensive data set on the temperature and rate-dependent properties of PA6, allowing the development of constitutive models. Different heating rate DSC measurements were conducted to calculate the crystallinity of the received material. Frequency sweep DMA was carried out to test the frequency (rate)- and temperature-dependent viscoelastic behaviour. Moreover, the DMA data were used to construct a master curve and estimate the activation energies of glass- and secondary-transitions. A DIC system was applied to tensile tests at two loading speeds to measure the inhomogeneous deformation process and thereby extract the local constitutive behaviour during large strain deformation. Temperature-dependent compression tests were performed at temperatures spanning the β- and α-transitions. Rate-dependent compression constitutive behaviours were measured using a screw-driven machine, hydraulic machine and SHPB from low to high strain rates; some tests were instrumented with a high-speed IR camera to investigate the effects of temperature rise on the mechanical performance during plastic deformation. Using these data, the true stress-strain curves obtained from representative points in tensile and compression tests are compared to further understand the strain localisation during the tensile tests. The rate- and temperature-dependent compression tests are also compared to enhance the time-temperature equivalence at small strains, and allow the effect of adiabatic heating on the large strain response to be addressed.

2. Material information and sample preparation

Injection moulded PA 6 sheets, Akulon® K222-D [32], were provided by DSM®. The dimensions of these sheets were approximately 300 × 100 × 2 mm, and they were provided in sealed bags, 'dry as moulded'. Test specimens were machined from these sheets, then immediately vacuum packed and stored in a freezer to minimise uptake of water. Specimens were returned to room temperature and then removed from the vacuum pack immediately before testing.

A number of specimen dimensions were used. Differential Scanning Calorimetry (DSC) samples were discs of about 3 mm diameter and 0.5 mm thickness. The Dynamic Mechanical Analysis samples were 60 mm in length, 10 mm wide and 2 mm thick, consistent with ASTM standard D4065. The tensile samples were cut according to ISO 527 type 1BA with 25 mm gauge length and 30 mm straight length, as shown in Fig. 1. Compression samples were cut through-thickness cut at the centre of the sheet and had 4 mm diameter and 2 mm thickness.

3. Experimental procedure

3.1. Differential scanning calorimetry (DSC)

DSC experiments were performed using a commercial DSC system, TA Instruments Q2000. Specimens were heated at 2, 5, 10, 20, 50 and 100 °C/min from −50 to 350 °C. The method of calculation of the crystallinity will be described in the next section.

3.2. Dynamic Mechanical Analysis (DMA)

Song et al. [26] compared the temperature dependent moduli of polycarbonate using a single cantilever beam and three three-point bend configuration. The results indicated that the three-point bend configuration could give more accurate moduli than a single cantilever beam – assessed by comparison with tensile test results. However, when the temperature is above the glass transition, pure amorphous polymers such as polycarbonate lose stiffness very rapidly, so that the loss modulus and tan delta peak cannot be captured using a three-point bend configuration because there is no clamp to hold the sample during the tests.

As a semi-crystalline polymer, PA 6 has residual stiffness above its glass-transition temperature: the DMA experiments in this paper were performed using a three-point bend configuration. A commercial DMA machine, TA Q800, was used. The apparatus and clamps were calibrated

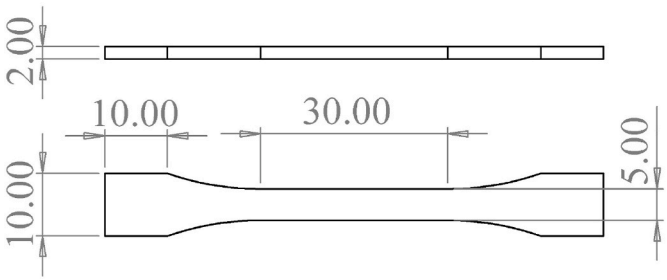

Fig. 1. Dimensions of tension sample (ISO 527 type 1BA).

before the tests, then isothermal frequency sweeps were performed at 2 °C increments from −100 to 110 °C, spanning the β- and α-transitions, with a 5-min equilibrium time at each temperature step. Oscillatory displacement with 0.1% strain amplitude was applied at frequencies of 0.1, 0.25, 1, 2.5 and 10 Hz with a 125% force track. The DMA data were used to construct a master curve (time-temperature superposition, TTS), and Arrhenius plots were used to estimate the activation energies of the α- and β-transitions.

3.3. Tension tests

An Instron 5980 universal test machine with a 100 kN load cell was employed to perform tensile tests at 25 and 5 mm/min loading speeds at room temperature. A high resolution CCD camera with a 105 mm lens was placed about 400 mm from the sample surface to capture the deformation process. To generate a speckle pattern for subsequent digital image correlation (DIC), the tensile bar was sprayed using water-based white ink, after which a black marker pen was used to create a random pattern of dots. During tests, the ink and dots adhered well to the specimens. More detailed information about DIC processing parameters can be found in Appendix A.

3.4. Compression tests

In this research, all strains in compression tests are reported as true strain, and the true stress was calculated based on the incompressible volume assumption.

Fig. 2 shows the experimental apparatus for the rate-dependent tests. Again, a screw-driven test machine, Instron 5980, with 100 kN load cell and compression anvils, was used to perform the tests at 0.001, 0.01, 0.1 and 0.5 s^{-1}. In these QS tests, an extensometer was attached to the loading anvils to minimise rig compliance effects (Fig. 2(a)). The measurement from this extensometer was used to allow true strain rate control during the experiment, and to provide strain measurements for subsequent analysis. An environmental chamber was used to perform temperature-dependent QS tests, the high temperature environment was created using a heating element, and liquid nitrogen was used to lower the temperature. Petroleum jelly was used to reduce the friction effects at room temperature and high temperatures, as suggested in Ref. [33], and AEROSPEC® 210 graphited grease was used in the low-temperature tests.

Experiments at rates around 10 s^{-1} were conducted on a custom-built hydraulic machine (Fig. 2(b)), which is made from a hydraulic actuator, a strain gauge-based force transducer and two linear variable differential transformers (LVDTs). The displacement or strain was obtained from the averaged two LVDT signals, and the stress was converted from the force transducer.

Fig. 3(c) shows the schematic of the split Hopkinson pressure bar (SHPB) used for high strain rate experiments. This can generate a strain rate from 1500 to 6000 s^{-1} with a final true strain above 1. A gas gun launches the Ti-6AL-4V striker bar to generate the input wave in the input bar, and this input stress wave is propagated along the input bar to the specimen, which is sandwiched between the Ti-6AL-4V input and output bars. The change in impedance at the bar-sample interface causes some of the stress wave to be transmitted into the output bar, and the remainder to be reflected back into the input bar. The input and reflected waves are measured using the strain gauges attached to the input bar, and the transmitted wave can be obtained from the strain gauges on the output bar. The stress-strain relationship is produced using standard equations described in Ref. [34]. A thin brass film was used as a pulse shaper to reduce the wave oscillations caused by the dispersion of high frequency waves in the bars, and petroleum jelly was used as lubrication to reduce the friction between the sample-bar interface. More details of testing polymers using the SHPB system can be found in reviews by Siviour and Jordan [17,35].

A Telops M3k IR camera mounted with a 50 mm lens and 0.75 inch extension ring was used to measure the temperature rise in the specimens at 0.1, 0.5, 12 and 3000 s^{-1} at room temperature. For the tests at strain rates lower than 100 s^{-1}, the frame rate of the IR camera is sufficient to allow continuous high-resolution thermal images during tests. For high rate tests, the frame rate is insufficient to record an adequate number of thermal images during a single experiment, which has a duration of approximately 400 μs Thus, the 'shift and reconstruction' method has been developed to stitch together thermal images from several high-rate tests and construct a 'continuous' sequence of thermal images at different strains; more details are given in the later section. Before testing, the camera factory default calibration was verified using a calibrated black body source between 50 and 150 °C. The emissivity of PA 6 is taken as 0.965, as described in the literature [36]. More details of the IR camera settings used are given in Table 1.

4. Experimental results – thermomechanical properties

4.1. DSC measurements

Fig. 3(a) shows the heat flow (W g^{-1}) as a function of temperature for six different heating rates. Here, data between 100 and 250 °C are shown because the endothermic peaks occurred in this region. Fig. 3(b) gives an example of how the percentage of crystallinity was calculated. Firstly, all curves were converted to J g^{-1} $°C^{-1}$. Secondly, the curves were zeroed; all curves showed a small exothermic peak followed by a large endothermic heat flow, indicating some recrystallization followed by melting [37].

To find the intrinsic crystallinity of the received material at room temperature, the curves were integrated from 150 °C to 250 °C. The crystallinity (X_c) of the received material is [2,37]:

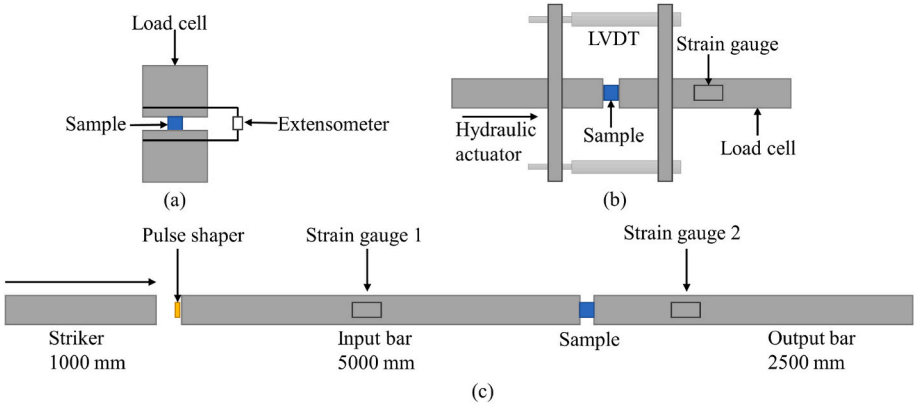

Fig. 2. Experimental apparatus (a) Screw-driven quasi-static compression (b) Medium rate hydraulic compression (c) High rate split Hopkinson pressure bar.

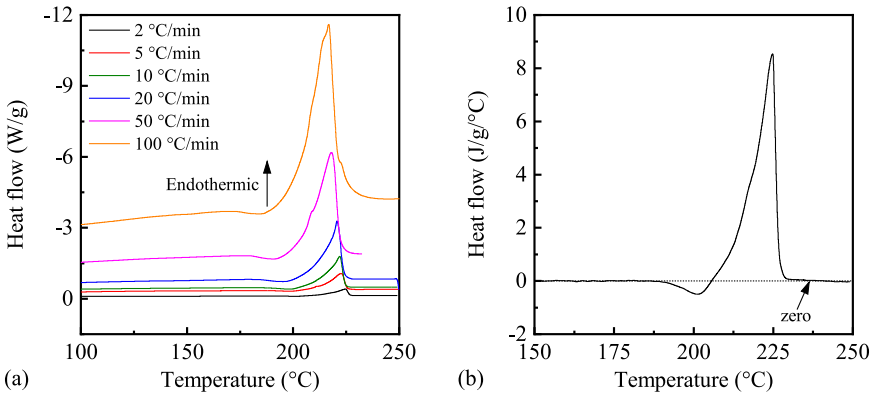

Fig. 3. (a) Heat flow (W g^{-1}) against temperature using different heating rates (b) Example (2 °C/min) of melting energy.

Table 1
IR camera settings for all experiments.

Strain rate	Frame rate (Hz)	Exposure time (μs)	Window size (pixel^2)
Low rate	100	100	128 × 128
Medium rate	500	100	300 × 160
High rate	10,000	20	92 × 128

$$X_c = \frac{\Delta H_m}{\Delta H_f^0} \tag{1}$$

where, ΔH_m is different between the measured heat of fusion and the heat of crystallization during the DSC scan. ΔH_f^0 is a reference value indicating heat of melting 100% crystalline polymer; a value of about 230 J g^{-1} for PA 6 was obtained from the literature [37,38].

Table 2 shows the percentage crystallinity of PA 6 measured using different heating rates. For the heating rates between 2 and 20 °C/min, the values are approximately 27%, which is in the expected range (25–35%) for injection moulded PA 6 [39].

4.2. DMA measurements

The original data for storage and loss modulus are shown in Fig. 4(a). Both frequency and temperature can affect these moduli; an increase in frequency can increase the storage modulus; the storage modulus decreases with an increased temperature and shows three stages: (1) from −100 to about −50 °C, the E' value presented a dramatic drop because of the secondary (β)-transition effects; (2) from −50 to about 35 °C, E' showed a plateau; (3) above 35 °C, E' exhibited a very rapid drop because of the glass (α)-transition. Here, as a semi-crystalline polymer, the crystal phase of PA 6 can provide residual stiffness when the temperature is above the glass-transition temperature, and this gives a chance to capture the loss modulus peak and Tan delta peak of the α-transition using the three-point bend configuration, as well as to calculate the transition activation energies.

Fig. 4(b) shows a master curve of E' versus logarithm strain rate, obtained using time-temperature superposition (TTS). Here, the strain rate is used to allow easier comparison to the compression data presented later, and is estimated as [17]:

$$\dot{\varepsilon} \approx \frac{\Delta \varepsilon}{\Delta t} = \frac{\varepsilon_0}{1/4f} = 4f\varepsilon_0 \tag{2}$$

Table 2
Calculated percentage crystallinity of PA 6 specimens.

Heat rate (°C/min)	2	5	10	20	50	100
Crystallinity (%)	27.9	27.0	26.6	27.8	24.6	25.9

where, f and ε_0 are applied frequency and strain amplitude in the DMA test. The fundamental principle of TTS is that an increase in frequency and a lowering in temperature have a similar effect on polymer materials. The horizontal shifting algorithm moves the isotherms at temperatures above the reference temperatures (20 °C) to lower frequencies, and those at temperatures below the reference temperature to higher frequencies. Therefore, each isotherm overlaps its neighbours and forms the master curve. In this study, these shifts were performed manually, more details about the shifting can be found in Refs. [40,41], and the shift factors as a function of temperature are shown in Fig. 4(c).

Two distinct peaks can be observed in the loss modulus (Fig. 4(a)) and Tan delta curves (data available online): at low temperatures, the β-transition peaks occurred from −80 to −55 °C; at high temperatures, the α-transition peaks were between 46 and 60 °C. All these transitions are frequency (rate)-dependent; a higher frequency will move the transition peak to a higher temperature. To calculate the activation energies, the Arrhenius equation is applied:

$$\ln(f) = \ln(A) - \frac{E_a}{R}\frac{1}{T} \tag{3}$$

where f is the frequency, A is the preexponential factor; E_a is the activation energy; R is the gas constant; and T is the absolute temperature. If base-10 logarithms are applied, the gradient of log(f) versus $1/T$ can be written as Equation (4) and plotted as Fig. 4(d).

$$k = -\frac{E_a}{2.303R} \tag{4}$$

The activation energy for the secondary (β)-transition and glass (α)-transition are 64.5 and 347 kJ mol^{-1} The different curve fitting methods can give different results for activation energy. All the raw DMA data can be found as online supplementary material using a DOI given at the end of this paper, and the reader can select a suitable method to calculate the activation energy for transitions according to model requirements.

4.3. Tension tests

Three tests were performed for each loading speed; the force-displacement curves are shown in Fig. 5(a). In this paper, one of the 25 mm/min tests (Fig. 5(b)) is used as an example to interpret the data analysis process and results, whilst results from a 5 mm/min test are shown in Appendix B.

The optical images were processed using the commercial software MatchID® (www.matchid.eu, version 2023.2.1) to obtain strain and strain rate information; the processing setup can be found in Appendix A. To investigate the strain localisation, five data points were picked from the centreline of the specimen, distributed evenly in the gauge area and labelled as A to E in Fig. 6. One more data point was selected,

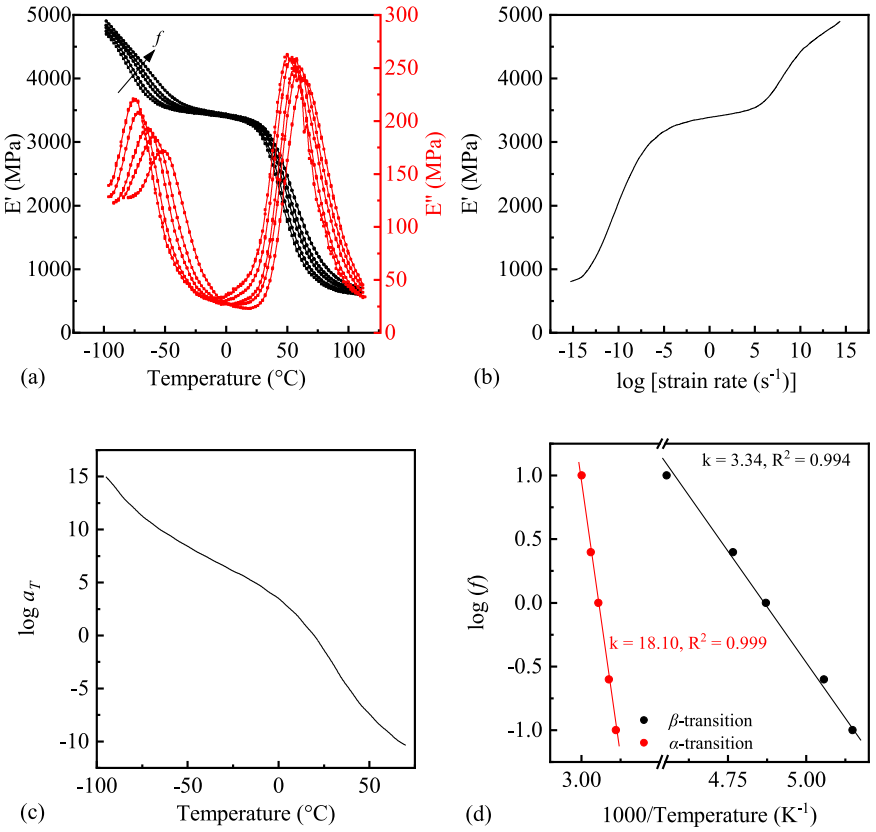

Fig. 4. Results from three-point bend frequency sweep DMA: (a) Original data for storage (E′) and loss (E″) modulus (b) Time-temperature superposition master curve (c) Shift factor against temperature (d) Arrhenius plot for α- and β-transition.

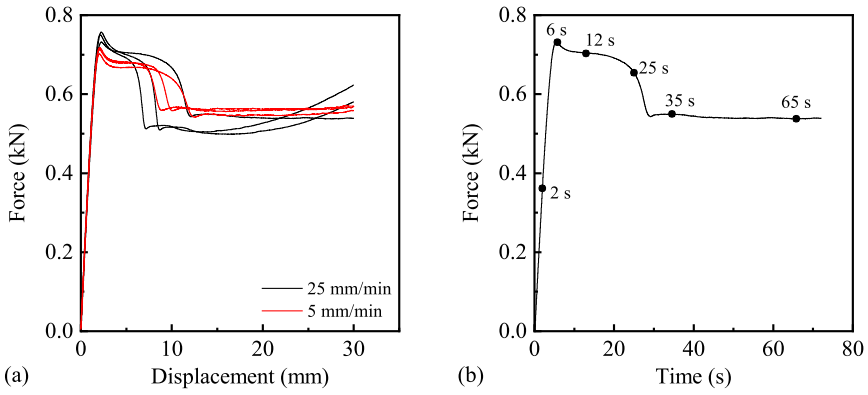

Fig. 5. (a) Force-displacement curves for tensile tests at speeds of 25 and 5 mm/min (b) Force-time curve for one of 25 mm/min test.

labelled as Neck, which indicated the position of first necking in the test. All strain-related data were processed as Hencky (true) strain and extracted at these points as functions of time.

Fig. 6 shows the contours of axial true strain generated by DIC for a 25 mm/min tension test at different times (Fig. 5(b)). From the beginning to 6 s, the force shows a linear relationship with displacement; correspondingly, there is no evident colour gradient in DIC strain mapping. Following the linear part, the force experiences a slight drop (after 6 s), and the strain curve shows a short plateau, which indicates that the whole gauge area deformed plastically and homogeneously until 25 s, when the force decreased significantly and pronounced localisation is observed in the true strain map. After that, the neck progressed through the gauge area, to encompass measurement points B and C.

Fig. 7 shows strain and strain rate versus time for the selected data points. Localisation initialises at the Neck point, causing a rapid increase in strain rate at this point; this then moves outwards from the neck through the specimen. At the moment of necking, more distant points experienced elastic unloading, which is seen as a negative strain rate in Fig. 7(b), and remain at a constant strain until the neck arrives (Fig. 7(a) and (b), point B).

To address the true stress, the strains in transverse and through-thickness directions, ε_{xx} and ε_{zz}, are required. This paper uses two methods, based on different assumptions, to estimate these so that the axial true stress (σ_{yy}) can be calculated. The strain in transverse and through-thickness directions was assumed to be the same: $\varepsilon_{xx} = \varepsilon_{zz}$, and

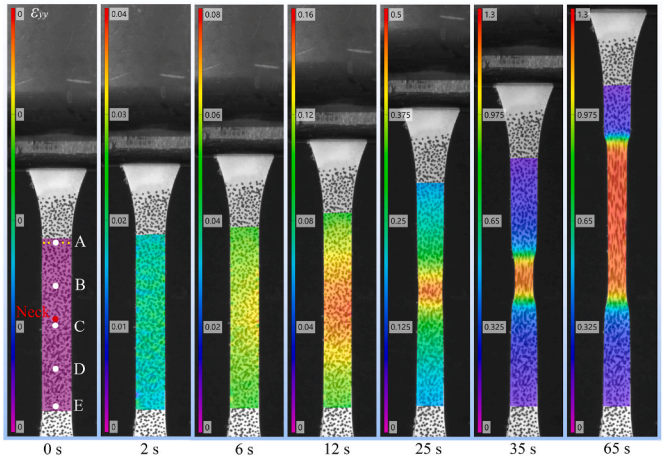

Fig. 6. Axial true strain maps for a 25 mm/min tension test obtained from DIC at different times, shown in Fig. 5(b).

the two methods were:

Method 1 (Fig. 8(a)): calculating ε_{xx} according to ε_{yy} assuming constant volume:

$$\varepsilon_{xx} = \varepsilon_{zz} = \frac{-\varepsilon_{yy}}{2} \tag{5}$$

$$\sigma_{yy} = \frac{F \times \exp(\varepsilon_{yy})}{A_0} \tag{6}$$

where, A_0 indicates the cross-sectional area of the undeformed sample.

Method 2 (Fig. 8(b)): using averaged overall transverse strain ε_{xx}:

$$\varepsilon_{xx} = \ln\left(\frac{x_r' - x_l'}{x_r - x_l}\right) \tag{7}$$

$$\sigma_{yy} = \frac{F}{A_0 \times \exp(2\varepsilon_{xx})} \tag{8}$$

Fig. 9 shows the axial true stress-true strain curves obtained from the two methods, and a comparison for three representative points. The yield points are the same; however, there are significant differences after further deformation. Immediately after yield, the strains along the specimen become non-uniform. There is no apparent softening, and at a strain of about 0.25, the Neck point experiences very rapid localisation, with a high strain rate, moving almost immediately to a high stress and strain. As the neck moves along the specimen, other points also experience rapid jumps in stress, which in Fig. 9(a) causes them to rejoin the same stress-strain curve as the neck. Points far from neck initiation, such as point A, do not experience this necking and cold drawing during this experiment.

To address the inconsistency of axial true stress calculated using the two different methods, the transverse and axial true strains, ε_{xx} and ε_{yy}, of the five points A-E, were extracted from DIC at different horizontal positions. It is noted that the horizontal width of the specimen is 5 mm; however, to minimise noise, a 4.5 mm wide region within this area was chosen, as shown in Fig. 10. Strains from points A, C and Neck are shown at six different times. Before the force drop (6 s), ε_{xx} is independent of position. Sequentially (12 s), point C (close to the Neck) and Neck experienced large deformation in the transverse direction compared with point A (far to the Neck); but the transverse strain is independent of horizontal location. Following that (25 s), point C and Neck showed more evident transverse strains (deformation) than point A; at the same time, the points closer to the edge experienced larger transverse strains than those in the centre. During the necking extension process (35 and 65 s), an apparent strain gradient can be found by comparing the edge

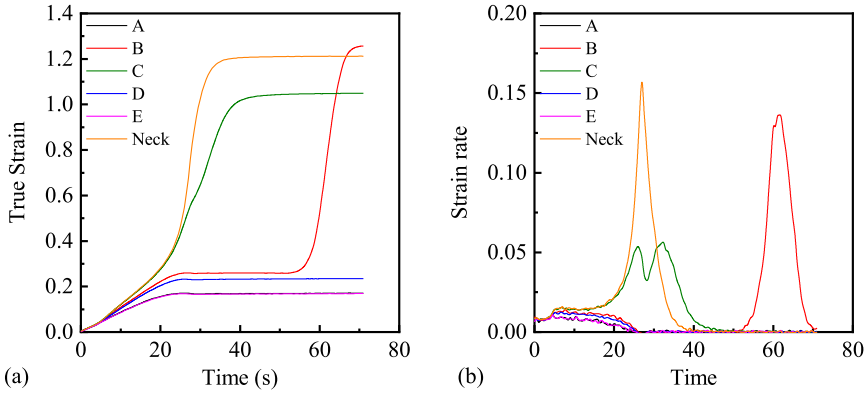

Fig. 7. Data extracted from six data (points A to E), which are evenly placed in gauge area, and one more data point (Neck) where the neck first formed (Fig. 6): (a) Axial true strain-time curve (b) Axial true strain rate-time curve.

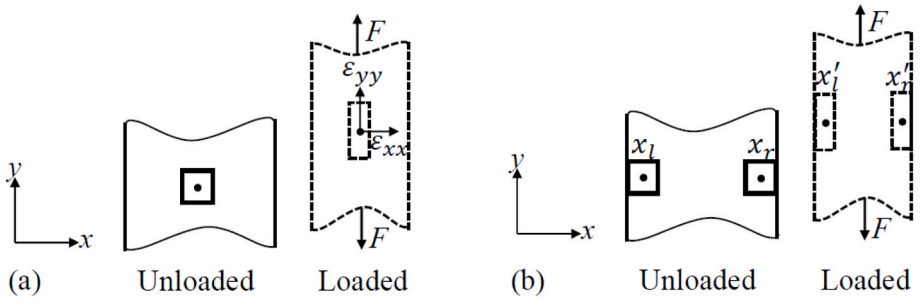

Fig. 8. Schematic of axial true stress calculation (a) Method 1 (b) Method 2 (reproduced from Ref. [13].

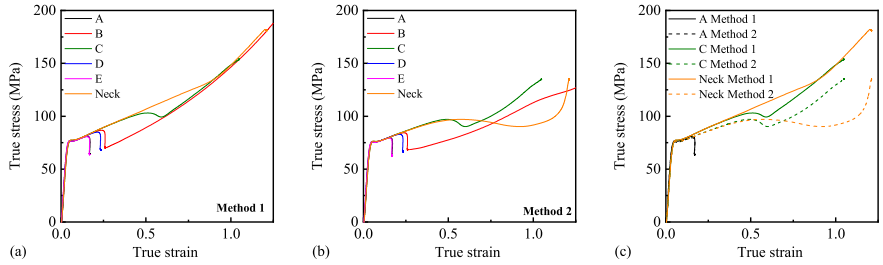

Fig. 9. Axial true stress-strain curves using (a) Method 1 (b) Method 2. (c) Comparison of true stress-strain curves of point A, point C, and neck obtained from different methods.

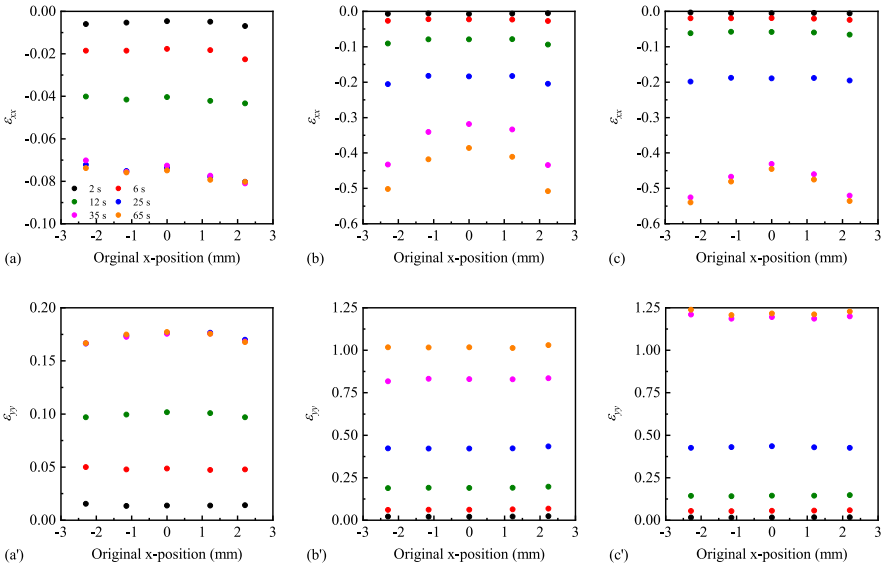

Fig. 10. Transverse true strain against original x-position for five points in the line of: (a) Point A (b) Point C (c) Neck. Axial true strain against original x-position for five points in the line of: (a') Point A (b') Point C (c') Neck. Note the different vertical scales for (a) and (a').

and centre points for both point C and Neck; this might be why Method 1 gives higher stress than Method 2. It is worth noting that the deformations in the axial (loading) direction for the points on the same horizontal line are very close to each other, as shown in Fig. 10(a'), (b') and (c').

There is no suitable method to verify whether the deformation in transverse and through-thickness directions are the same using 2D-DIC. Moreover, it is very challenging to understand the constitutive behaviour of material using remote data from tests with localisation. Thus, further tensile tests were not performed in this study. However, the tests performed do give important data for the validation of future material models.

4.4. *Varying rate and temperature compression tests*

For all QS tests, an approximately 5 N pre-load was applied to the samples to avoid 'toe-in'. Fig. 11(a) presents the true stress-true strain curves at starting temperatures from −60 to 200 °C, which covered the β- and α-transitions. Not all curves have a distinct yield peak on the temperature-dependent stress-strain curve, thus, Fig. 11(b) plots the

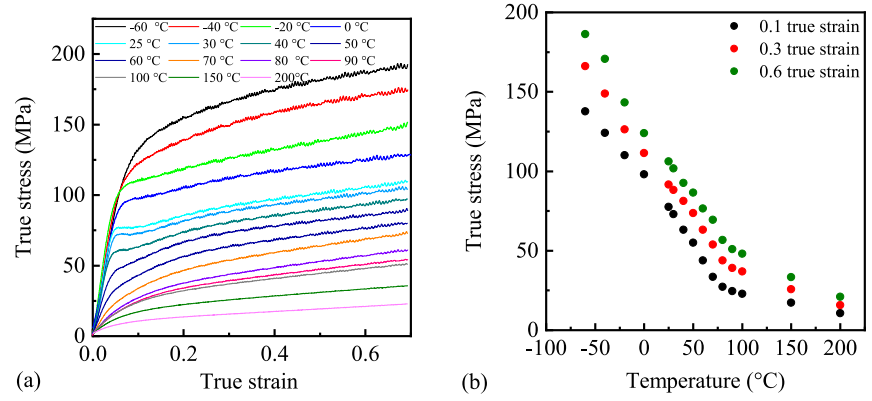

Fig. 11. Varying temperature compression tests (a) True stress-strain curves (b) True stresses at 0.1, 0.3 and 0.6 true strain against logarithm strain rate.

true stress at true strains of 0.1, 0.3 and 0.6. It can be seen that the stress increases with decreasing temperature for all strains. Moreover, the rate of increase is slightly higher at low temperatures because of the β-transition. The inflection at about 50 °C is a result of the glass transition.

Rate-dependent compression data are shown in Fig. 12(a). As for decreasing temperature, increasing strain rate strengthens the material, exhibiting the well-known time-temperature equivalence between temperature and strain rate. Fig. 12(b) plots the true stress at 0.1, 0.3 and 0.6 true strain as a function of the logarithm strain rate. At 0.1 true strain, the stress shows a bilinear increase with increasing strain rate, which again results from the β-transition effect. When the strain rate is or lower than 0.5, an apparent strain hardening is observed; however, when the strain rate is above 0.5, the strain hardening is barely seen. Correspondingly, the stress at large strain (0.3 and 0.6) is very close to that at 0.1 true strain when the strain rate is higher than 0.5 s^{-1} in Fig. 12(b). These observations are caused by the adiabatic heating effects, which will be addressed later.

4.5. Comparison of tension and compression data

Fig. 13(a) compares true stress-true strain curves obtained from the Neck points (Method 1) in tension and two true rate-controlled compression tests. The 5 mm/min tensile test and 0.001 s^{-1} compression test overlap very well, and the 25 mm/min tensile test and 0.01 s^{-1} true rate-controlled compression test are consistent until 0.3 true strain, after which they separate. Further exploring these observations, the true strain rate versus true strain curves for these four tests are plotted in Fig. 13(b). For the two tensile tests, in the beginning, the true strain rate experienced a sharp increase, which is the linear part of the force-displacement curves (first 6 s in Fig. 5(b) and first 25 s in Fig. B1); following that, plateaus start until a strain of about 0.25; these correspond to the plateaus after the first distinct peak in the force-displacement curves. After the plateaus, the strain rates in the tensile tests dramatically increase, which might result in inconsistent observed behaviour in tension and compression. This demonstrates, again, that even if local data are obtained, the tensile test is affected by both material constitutive and specimen geometry structural behaviour. Thus, both local (true strain-time curve) and global (force-displacement curve) behaviours should be considered when the tensile test is used to calibrate the constitutive parameters.

5. Experimental results – temperature rises during deformation

5.1. Motivation

Fig. 14 compares the large strain behaviour of temperature and rate-dependent compression tests with similar yield (inflection) stress. The rate-dependent (red lines) tests present evident softening compared with the temperature-dependent (black lines). During the large strain deformation, plastic work can be converted to heat, which at high strain rates does not have time to conduct out of the specimen. This self-heating can cause thermal softening at large strains. In order to investigate this further, a series of experiments was performed using an IR camera to measure the temperature rises in the specimens.

5.2. Low and medium rate experiments

Experiments were performed at rates of 0.1, 0.5 and 12 s^{-1}. Appendix C shows a discussion of the thermal conditions at these rates. Fig. 15 presents representative thermal images at strains of 0.1, 0.3, 0.5 and 0.7. For later comparison, the temperature was averaged over the white solid box in Fig. 15(a), allowing comparisons of stress and temperature against strain, Fig. 16. The fixed position and dimension of this average window was chosen to ensure that the temperature within this window was not significantly affected by the thermal conduction between the loading anvils and samples according to Appendix C, and can continuously represent the 'hottest' part of samples during the change of sample dimensions.

The temperature rises at these three strain rates are very close at strains below 0.2; following that, they diverge until the end of the tests. There is little plastic (or viscoelastic) work at the beginning of these tests; as the materials experience plastic deformation, generating heat which, at the highest rates of 12 s^{-1}, does not have sufficient time for significant heat conduction out of the specimen. Thus, more evident softening can be observed at higher strain rates. In the experiment at 12 s^{-1}, the eventual temperature rise is 20 °C, taking the total temperature higher than 40 °C, and moving the sample into the glass transition region. Appendix C investigates the thermal boundary conditions, and builds up phenomenological models [42] of tests at 12 and 0.5 s^{-1} strain rates to help interpret the experimental observations.

5.3. High strain rates

In high rate tests with the IR camera, the long split Hopkinson bar (LSHPB) was used multiple times at the same strain rate to produce consistent true stress-strain curves, as shown in Fig. 17 (a). At the same time, the IR camera triggering delay was altered in each test, allowing a series of images to be constructed by stitching single tests together. Fig. 17(b) shows an example of stitching of two LSHPB shots; the force signals overlap very well, and the IR triggering output signal indicates the IR camera recorded the thermal images at different moments. Thus, a continuous temperature mapping at different strains (Fig. 17(c)) can be constructed using 4–5 thermal images obtained from each test.

Fig. 17(d) shows the representative thermal images from yield (0.1 strain) to a very large strain. A significant temperature rise is observed

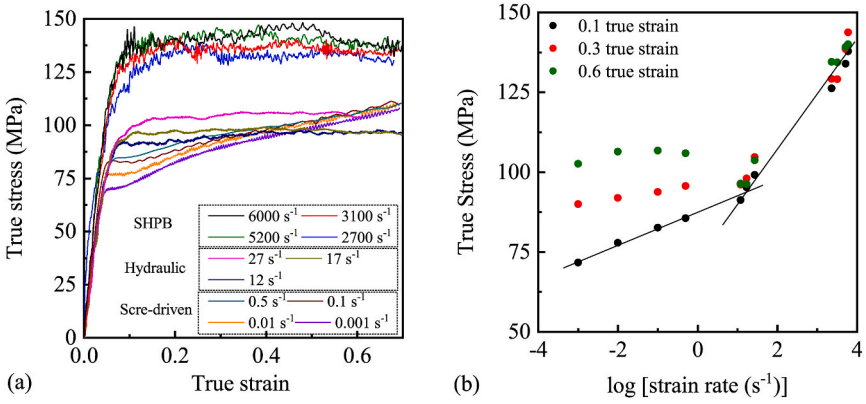

Fig. 12. Varying rate compression tests (a) True stress-strain curves (b) True stresses at 0.1, 0.3 and 0.6 true strain against logarithm strain rate.

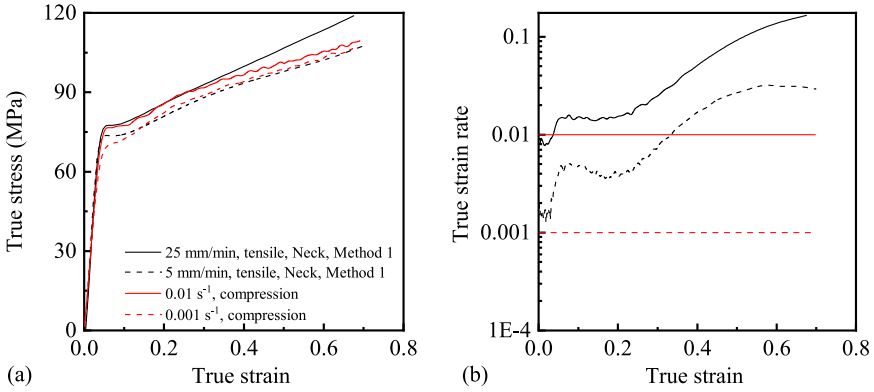

Fig. 13. Comparison between tension (point Neck, Method 1) and compression tests (a) true stress-strain curves and (b) true strain rate-strain curve.

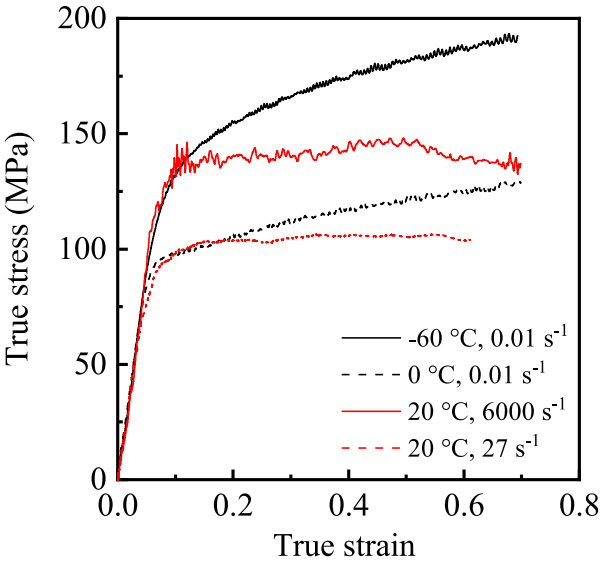

Fig. 14. Comparison of true stress-strain curves at low temperature and high strain rate tests.

during the deformation process. In particular, at a strain of 0.5, the temperature is about 40 °C, which moves the sample into its glass-transition region. Furthermore, with increased strain, more plastic

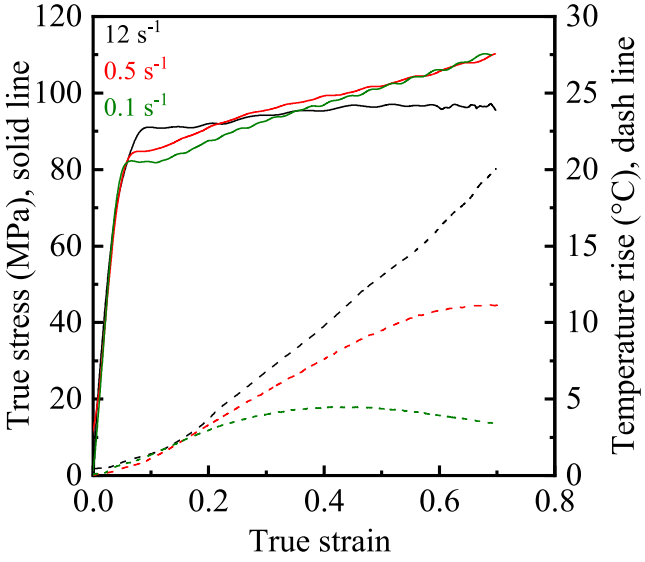

Fig. 16. True stress and corresponding temperature rise against true strain in three strain rate compression tests.

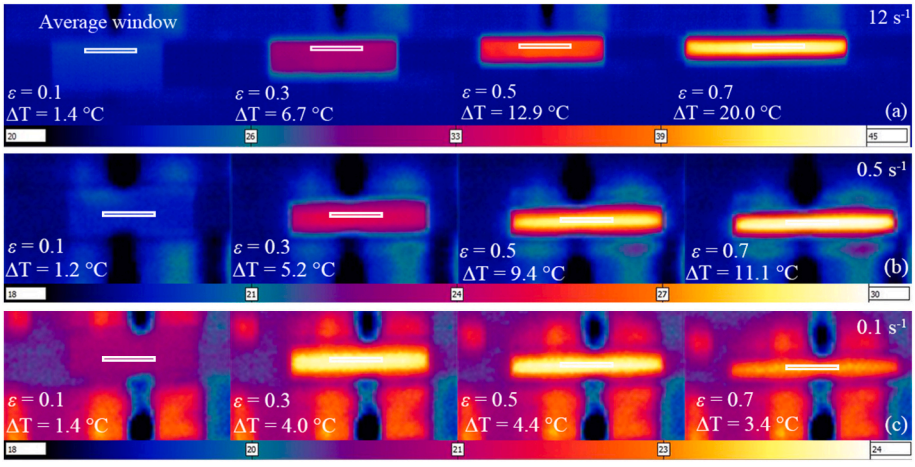

Fig. 15. Selected thermal images from experiments at (a) 12 s^{-1} (b) 0.5 s^{-1} (c) 0.1 s^{-1}.

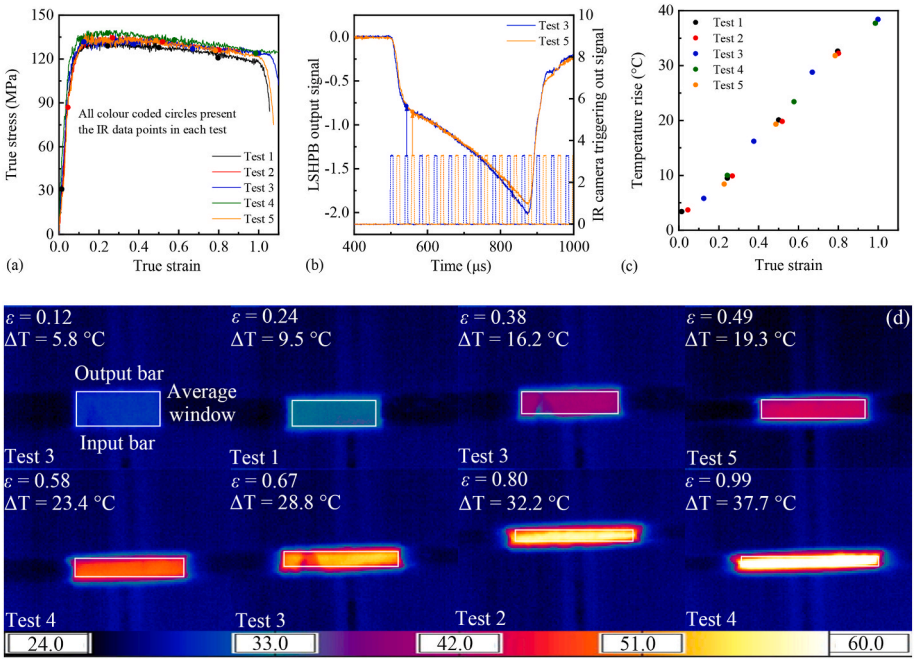

Fig. 17. (a) True stress versus true strain curves for five experiments on PA6 at 3000 s^{-1} (b) Time-shifted IR camera triggering out signal and LSHPB output bar signal from two experiments (c) Mean temperature rise versus true strain for all the images obtained from five tests (d) Representative thermal images from low to high strain.

work was converted to heat, and the temperature was about 60 °C at a true strain of 1.

6. Conclusions

Thermomechanical characterisation has been performed on dry polyamide 6 to provide a comprehensive dataset of mechanical properties. Results from the DSC measurements with different heating rates indicate that the crystallinity of received PA 6 is about 27 %, which is within the reported range of the commercial product. Frequency sweep DMA data shows frequency (rate)- and temperature-dependent moduli in the viscoelastic regions, and the secondary (β)- and glass (α)-transition peaks were observed in loss modulus and Tan delta. Moreover, the isotherms from DMA measurements were used to construct a master curve, which can predict the moduli at a strain rate regime far beyond the capability of the DMA machine. Then, the activation energies of these two transitions were calculated using the Arrhenius relationship.

Tensile tests were performed at two loading speeds, with full-field optical images that were processed using Digital Image Correlation to understand strain localisation. The tensile sample experiences viscoelastic deformation before the first force peak, and then the test moves to global plastic deformation at a constant stress, followed by apparent strain localisation, or necking with a significant force drop; finally, the neck extends to the rest of gauge area; this corresponds to a force plateau even though the true stress in the material is increasing. These observations demonstrate that the global behaviour (force-displacement curve) alone is insufficient to validate the constitutive parameters using the tensile test.

Compression tests were performed at a wide temperature and strain rate range to address the temperature- and rate-dependent behaviours of PA 6. Moreover, a high-speed IR was used to measure temperature rise in the tests at strain rates of 0.1, 0.5, 12 and 3000 s^{-1}. It can be seen that an increase in strain rate and a decrease in temperature can strengthen the material at small strains, which is consistent with the time-temperature equivalence theory of polymers. However, with the increasing strain rate, heating of the specimen leads to obvious thermal softening at large strains in medium and high rate tests.

Overall, this paper provides the first comprehensive study on the thermomechanical response of dry polyamide 6 at low and high strain rates, with valuable data for the development of constitutive models of semi-crystalline polymers.

CRediT authorship contribution statement

Peihao Song: Writing – original draft, Methodology, Investigation, Formal analysis, Data curation, Conceptualization. **Akash Trivedi:** Writing – review & editing, Formal analysis, Data curation, Conceptualization. **Nicholas Hawkins:** Formal analysis, Data curation. **Aaron Graham:** Investigation, Formal analysis. **David Chapman:** Writing – review & editing, Investigation, Conceptualization. **Clive R. Siviour:** Writing – review & editing, Supervision, Project administration, Investigation, Funding acquisition.

Declaration of competing interest

The authors declare that they have no known competing financial interests or personal relationships that could have appeared to influence the work reported in this paper.

Data availability

All data supporting this study are openly available from the Oxford University Research Archive at DOI 10.5287/ora-rygozwxov.

Acknowledgements

This research forms part of the research programme of DPI, project 827t19, *Impact Modelling of Polymers: high-Rate Experiments for Solid-state Simulations*. The authors thank our industrial partner DSM for supporting materials in this project, and we also thank Dr. Lucien Douven and Dr. Tom Engels for their valuable suggestions. We thank the Hypersonics Research Group for using the high speed thermal imaging camera, and EPSRC for supporting thermomechanical characterisation as part of EP/V003321/1. We gratefully acknowledge our colleagues on this project,

Dr. Davide De Focatiis and Grace Owen at the University of Nottingham for their helpful discussions. We also thank the technicians of the Solid Mechanics Group workshop, in particular Andy Bateman, for his help with the manufacture of specimens and fixtures for this project.

Appendix A. Digital image correlation setup

Table A1
Digital image correlation setup

Loading speeds (mm/min)	25	5
Camera (Point Grey)	GS3-U3-120S6M-C	
Image resolution (pixel)	4240 × 2824, 16-bit	
Frame rate (frame/s)	2	1
Lens	Nikon 105 mm Lens	
Field of view (pixels)	800 × 2824	
Pixel to mm conversion	0.024	
Stand-off distance (mm)	400	
Speckle size (pixels)	≈8	
DIC software	MatchID, version 2023.2.1	
Image filtering	Gaussian, 5 × 5 pixel kernel	
Subset size (pixel)	49	
Step size (pixel)	3	
Subset shape function	Quadratic	
Matching criterion	Zero-normalized sum of square differences (ZNSSD)	
Interpolant	Bicubic polynomial interpolation	
Strain tensor	Hencky (True) strain tensor	
Estimates progress history	Spatial and updated reference	
Strain window size	15 × 15 pixels^2, Quadratic Quadrilateral	

Appendix B. 5 mm/min tensile test data

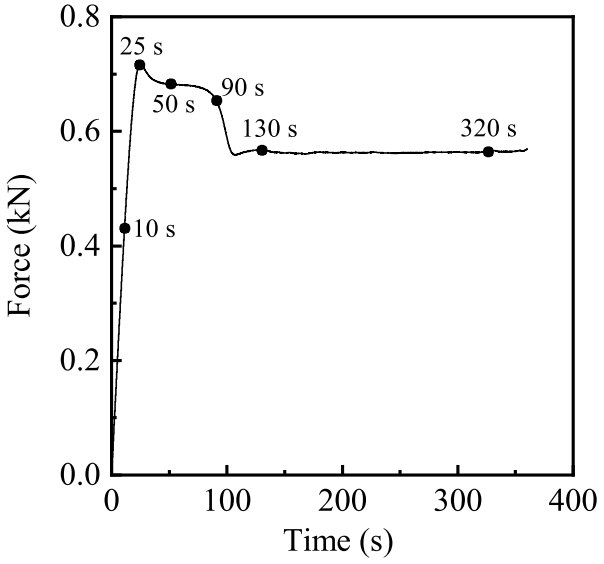

Fig. B1. Force-displacement curve from a 5 mm/min tension test.

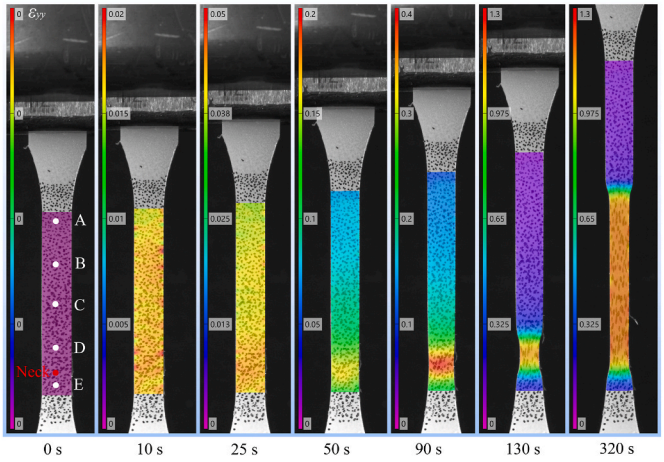

Fig. B2. Axial true strain maps for a 5 mm/min tension test obtained from DIC at different times (Fig. B1).

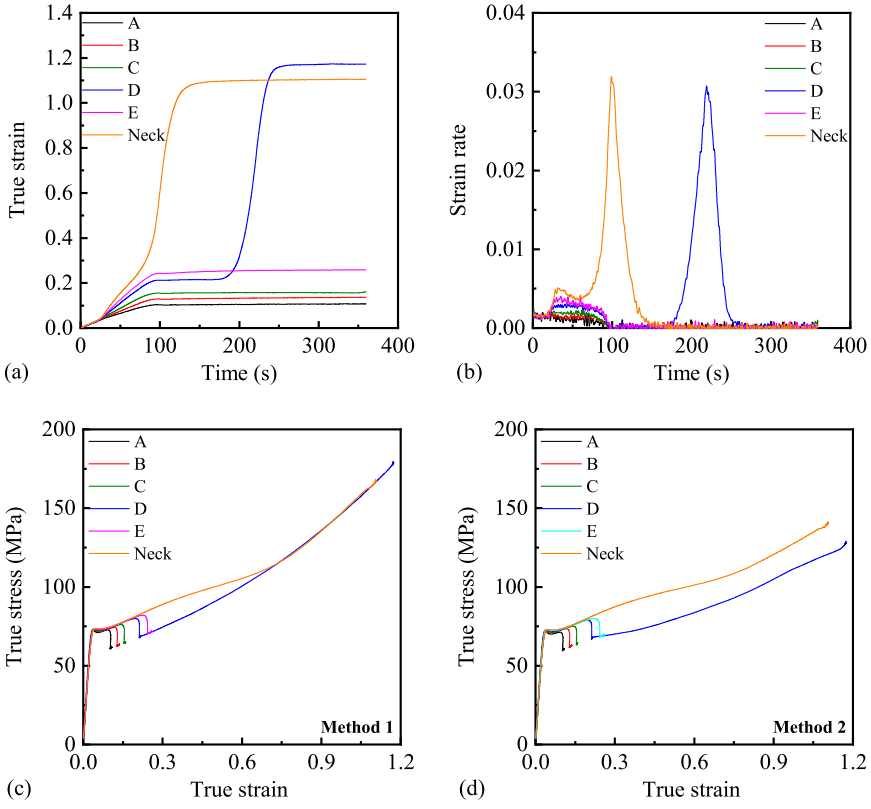

Fig. B3. Data extracted from six data (point A to E), which are evenly placed in gauge area, and one more data point (Neck) where the neck first formed (Fig.B2): (a) Axial true strain-time curve (b) Axial true strain rate-time curve; Axial true stress-strain curves using: (c) Method 1 (d) Method 2

Appendix C. Study of thermal boundary conditions using the FE model [42]

The following 1-D equations can estimate the strain rate over which the thermal conditions transition between isothermal and adiabatic [26]:

$$\alpha = \frac{k}{\rho C_p} \tag{9}$$

$$l_t = 2\sqrt{\alpha t} \Rightarrow t = \frac{1}{\alpha}\left(\frac{l_t}{2}\right)^2 \tag{10}$$

$$\dot{\varepsilon} = \frac{1}{t} \tag{11}$$

where, α is the thermal diffusivity, the thermal conductivity k is 0.28 W m^{-1} K^{-1} [43], the density ρ is 1.13 g cm^{-3} [32], and the specific heat capacity

C_P is 1.7 J g^{-1} K^{-1} [44]. t indicates the timescale for thermal diffusion, and l_t is the current length of the specimen. Based on this estimate, we see that experimental conditions begin to approach adiabatic at rates above 0.1 s^{-1} for the initial sample geometry (l_t is 2 mm). However, in practice the specimen becomes shorter during the experiment, so significant heat loss can begin to occur at this rate. To obtain a more sophisticated understanding of this, Finite Element (FE) simulations were performed.

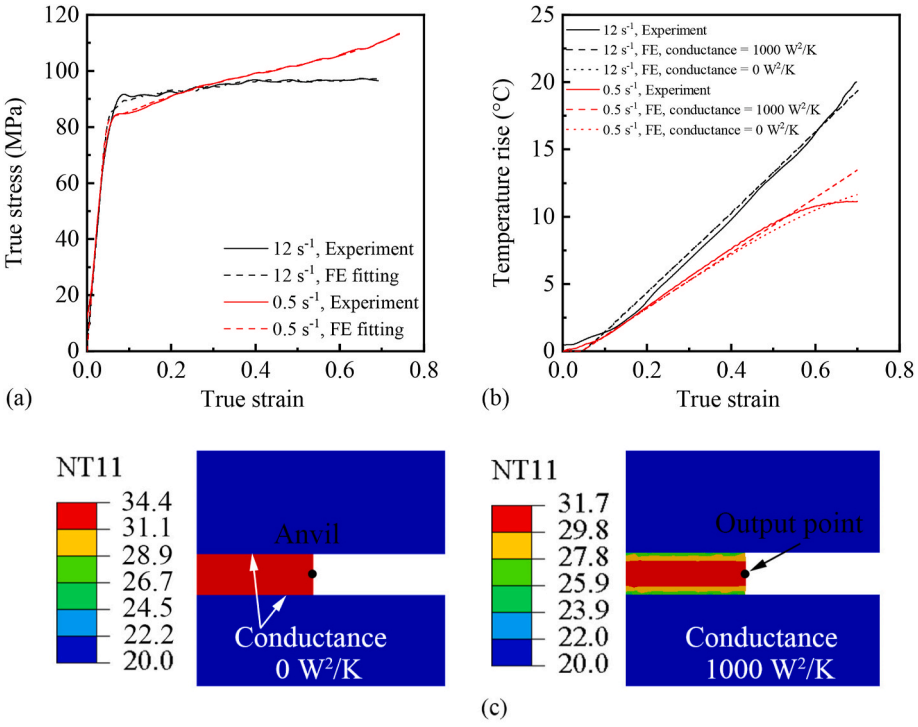

Fig. C1. (a) Experimental data and FE fitted true stress-strain curve at 0.5 and 12 s^{-1} in compression (b) Experimental data and FE output temperature rise-strain curves using different thermal conductance values (c) FE results for specimen temperature rise at 0.7 true strain for 0.5 s^{-1} compression tests using two conductance values.

To provide appropriate specimen behaviour in the FE simulation, the three-network viscoplastic (TNV) model from the PolyUMod® material library [42] was used to fit the true stress-true strain curves at 0.5 and 12 s^{-1} (Fig. C1(a), Table C1). In addition, the inelastic work fraction, which indicates the ratio of plastic work converted to heat, was defined to provide outputs consistent with experimental temperature rises. If the experimental condition is 'fully adiabatic', the temperature rise value should be independent of the thermal conductance value between sample-anvil interfaces. In Fig. C1(b), two conductance values are used to demonstrate the expected effect of conduction on the measured temperature rise: more detailed visualisation of the temperature distribution in the specimen is shown in C1(c) and (d). The results indicate that the test at 0.5 s^{-1} may be regarded as adiabatic to 0.5 true strain; and the test at 12 s^{-1} to 0.7 true strain.

Table C1
Curve fitting parameters using three-network viscoplastic [42] model used in Abaqus/Explicit

Description	Fitting parameters	
Material parameters of PA6	12 s^{-1}	0.5 s^{-1}
Density, ρ, (g/cm^3)	1.13 [32]	
Specific heat capacity, C_p, (J/(g °C)), at 20 °C	~1.70 [44]	
Thermal conductivity, K, (W/(m K))	0.28 [43]	
Inelastic heat fraction, TQC	0.50	0.65
Network A		
Yeoh parameter 1, C_{10}, (MPa)	5.5	11.4
Yeoh parameter 2, C_{20}, (MPa)	−3.0	−2.7
Yeoh parameter 3, C_{30}, (MPa)	0.83	0.90
Bulk modulus, κ_1, (MPa)	4377.5	
Bulk modulus, κ_2, (MPa)	0	
Bulk modulus, κ_3, (MPa)	0	
Network B		
Yeoh parameter 1, C_{10}, (MPa)	300.7	306.7
Yeoh parameter 2, C_{20}, (MPa)	0	
Yeoh parameter 3, C_{30}, (MPa)	0	
Bulk modulus, κ_1, (MPa)	4377.5	
Bulk modulus, κ_2, (MPa)	0	
Bulk modulus, κ_3, (MPa)	0	
Flow resistance of network, $\hat{\tau}$, (MPa)	58.8	66.9
Stress exponential of network, m	12.6	13.7
Volumetric flow coefficient, b	0	
Pressure dependent of flow, p_0	0	

(*continued on next page*)

Table C1 (*continued*)

Description	Fitting parameters	
Material parameters of PA6	12 s^{-1}	0.5 s^{-1}
Yield evolution of $\hat{\tau}$, f_f	1	
Yield evolution of characteristic strain, ε_f	0.1	
Flow damage strain, c_ε	0.1	
Flow damage final state, f_s	1	
Material parameters of loading anvils (Steel)		
Density, ρ, (g/cm^3)	7.85	
Specific heat capacity, C_p, (J/(g °C))	0.47	
Thermal conductivity, K, (W/(m K))	45	
Young's modulus, E, (MPa)	210,000	
Poisson's ratio	0.3	

References

[1] E. Parodi, G.W.M. Peters, L.E. Govaert, Prediction of plasticity-controlled failure in polyamide 6: influence of temperature and relative humidity, J. Appl. Polym. Sci. 135 (11) (2018) 45942.

[2] E. Parodi, L.E. Govaert, G.W.M. Peters, Glass transition temperature versus structure of polyamide 6: a flash-DSC study, Thermochim. Acta 657 (2017) 110–122.

[3] I. Kolesov, D. Mileva, R. Androsch, C. Schick, Structure formation of polyamide 6 from the glassy state by fast scanning chip calorimetry, Polymer 52 (22) (2011) 5156–5165.

[4] C. Millot, L.-A. Fillot, O. Lame, P. Sotta, R. Seguela, Assessment of polyamide-6 crystallinity by DSC, J. Therm. Anal. Calorim. 122 (1) (2015) 307–314.

[5] E. Parodi, G.W.M. Peters, L.E. Govaert, Structure-properties relations for polyamide 6, Part 2: influence of processing conditions during injection moulding on deformation and failure kinetics, Polymers 10 (7) (2018) 779.

[6] E. Laredo, M. Grimau, F. Sanchez, A. Bello, Water absorption effect on the dynamic properties of nylon-6 by dielectric spectroscopy, Macromolecules 36 (26) (2003) 9840–9850.

[7] G.-F. Shan, W. Yang, M.-b. Yang, B.-h. Xie, J.-m. Feng, Q. Fu, Effect of temperature and strain rate on the tensile deformation of polyamide 6, Polymer 48 (10) (2007) 2958–2968.

[8] L. Laiarinandrasana, N. Selles, O. Klinkova, T.F. Morgeneyer, H. Proudhon, L. Helfen, Structural versus microstructural evolution of semi-crystalline polymers during necking under tension: influence of the skin-core effects, the relative humidity and the strain rate, Polym. Test. 55 (2016) 297–309.

[9] R.P. Chartoff, J.D. Menczel, S.H. Dillman, Dynamic Mechanical Analysis (DMA), Thermal Analysis of Polymers: Fundamentals and Applications, 2009, pp. 387–495.

[10] K.P. Menard, N.R. Menard, Dynamic mechanical analysis in the analysis of polymers and rubbers, Encycl. Polym. Sci. Technol. (2002) 1–33.

[11] K.J. Laidler, The development of the Arrhenius equation, J. Chem. Educ. 61 (6) (1984) 494.

[12] E. Parsons, M.C. Boyce, D.M. Parks, An experimental investigation of the large-strain tensile behavior of neat and rubber-toughened polycarbonate, Polymer 45 (8) (2004) 2665–2684.

[13] P. Song, A. Trivedi, C.R. Siviour, Tensile testing of polymers: integration of digital image correlation, infrared thermography and finite element modelling, J. Mech. Phys. Solid. 171 (2023) 105161.

[14] F. Grytten, H. Daiyan, M. Polanco-Loria, S. Dumoulin, Use of digital image correlation to measure large-strain tensile properties of ductile thermoplastics, Polym. Test. 28 (6) (2009) 653–660.

[15] M. Lei, C.M. Hamel, K. Chen, Z. Zhao, H. Lu, K. Yu, H.J. Qi, Thermomechanical behaviors of polyether ether ketone (PEEK) with stretch-induced anisotropy, J. Mech. Phys. Solid. 148 (2021) 104271.

[16] R. Zhang, P. Bai, D. Lei, R. Xiao, Aging-dependent strain localization in amorphous glassy polymers: from necking to shear banding, Int. J. Solid Struct. 146 (2018) 203–213.

[17] C.R. Siviour, J.L. Jordan, High strain rate Mechanics of polymers: a review, J. Dyn. Behav. Mater. 2 (1) (2016) 15–32.

[18] M.J. Kendall, C.R. Siviour, Experimentally simulating adiabatic conditions: approximating high rate polymer behavior using low rate experiments with temperature profiles, Polymer 54 (18) (2013) 5058–5063.

[19] S.M. Walley, J.E. Field, Strain rate sensitivity of polymers in compression from low to high rates, DYMAT j. 1 (3) (1994) 211–227.

[20] M. Plöckl, Effect of Strain Rate on the Tensile, Compressive, and Shear Response of Carbon-Fiber-Reinforced Thermoplastic Composites, 2019.

[21] H. Pouriayevali, S. Arabnejad, Y.B. Guo, V.P.W. Shim, A constitutive description of the rate-sensitive response of semi-crystalline polymers, Int. J. Impact Eng. 62 (2013) 35–47.

[22] M.I. Okereke, C.P. Buckley, C.R. Siviour, Compression of polypropylene across a wide range of strain rates, Mech. Time-Dependent Mater. 16 (4) (2012) 361–379.

[23] P.J. Rae, E.N. Brown, E.B. Orler, The mechanical properties of poly(ether-ether-ketone) (PEEK) with emphasis on the large compressive strain response, Polymer 48 (2) (2007) 598–615.

[24] E.N. Brown, R.B. Willms, G.T. Gray, P.J. Rae, C.M. Cady, K.S. Vecchio, J. Flowers, M.Y. Martinez, Influence of molecular conformation on the constitutive response of polyethylene: a comparison of HDPE, UHMWPE, and PEX, Exp. Mech. 47 (3) (2007) 381–393.

[25] C.R. Siviour, S.M. Walley, W.G. Proud, J.E. Field, The high strain rate compressive behaviour of polycarbonate and polyvinylidene difluoride, Polymer 46 (26) (2005) 12546–12555.

[26] P. Song, A.R. Trivedi, C.R. Siviour, Mechanical response of four polycarbonates at a wide range of strain rates and temperatures, Polym. Test. 121 (2023) 107986.

[27] D. Rittel, On the conversion of plastic work to heat during high strain rate deformation of glassy polymers, Mech. Mater. 31 (2) (1999) 131–139.

[28] M.J. Kendall, C.R. Siviour, Experimentally simulating high-rate behaviour: rate and temperature effects in polycarbonate and PMMA, Phil. Trans. Math. Phys. Eng. Sci. 372 (2015) (2014) 20130202.

[29] A.R. Trivedi, P. Song, C.R. Siviour, Experimentally simulating adiabatic behaviour: capturing the high strain rate compressive response of polymers using low strain rate experiments with programmed temperature profiles, Polym. Test. 116 (2022) 107773.

[30] S.M. Walley, W.G. Proud, P.J. Rae, J.E. Field, Comparison of two methods of measuring the rapid temperature rises in split Hopkinson bar specimens, Rev. Sci. Instrum. 71 (4) (2000) 1766–1771.

[31] G.G. Goviazin, A. Shirizly, D. Rittel, A comparative study of the performance of IR detectors vs. High-speed cameras under dynamic loading conditions, Exp. Mech. 63 (1) (2023) 115–124.

[32] DSM, Akulon® K222, D Data Sheet, 2023.

[33] A. Trautmann, C.R. Siviour, S.M. Walley, J.E. Field, Lubrication of polycarbonate at cryogenic temperatures in the split Hopkinson pressure bar, Int. J. Impact Eng. 31 (5) (2005) 523–544.

[34] G.T. Gray-III, Classic split-Hopkinson pressure bar testing, ASM Handbook, Mech. Testing Evaluation 8 (2000) 462–476.

[35] C.R. Siviour, High strain rate characterization of polymers, AIP Conf. Proc. 1793 (1) (2017).

[36] F. Steiner, F. Bleicher, M. Klingenbrunner, Emissivity Factor of Thermoplastic Materials for a Robot Bending Process, 2016, pp. 664–670.

[37] Y.P. Khanna, W.P. Kuhn, Measurement of crystalline index in nylons by DSC: complexities and recommendations, J. Polym. Sci. B Polym. Phys. 35 (14) (1997) 2219–2231.

[38] B. Wunderlich, Macromolecular Physics: Crystal Melting, Academic Press, 2013.

[39] R. Seguela, Overview and critical survey of polyamide6 structural habits: misconceptions and controversies, J. Polym. Sci. 58 (21) (2020) 2971–3003.

[40] A.R. Trivedi, C.R. Siviour, A novel methodology for predicting the high rate mechanical response of polymers from low rate data: application to (plasticised) poly (vinyl chloride), Mech. Time-Dependent Mater. 25 (2021) 383–409.

[41] S.-h. Yoon, I. Giannakopoulos, C.R. Siviour, Application of the Virtual Fields Method to the uniaxial behavior of rubbers at medium strain rates, Int. J. Solid Struct. 69 (2015) 553–568.

[42] J.S. Bergstrom, PolyUMod–A library of advanced user materials. Veryst Engineering, LLC, Needham, Mass, USA, 2012.

[43] Y. Ren, Y. Zhang, H. Guo, R. Lv, S.-L. Bai, A double mixing process to greatly enhance thermal conductivity of graphene filled polyamide 6 composites, Compos. Appl. Sci. Manuf. 126 (2019) 105578.

[44] J.R. Asay, S.R. Urzendowski, A.H. Guenther, Ultrasonic and Thermal Studies of Selected Plastics, Laminated Materials, and Metals, Air Force Weapons Laboratory, 1968.